

See discussions, stats, and author profiles for this publication at: <https://www.researchgate.net/publication/51100777>

Local-Mode Approach to Modeling Multidimensional Infrared Spectra of Metal Carbonyls

ARTICLE *in* THE JOURNAL OF PHYSICAL CHEMISTRY A · JUNE 2011

Impact Factor: 2.69 · DOI: 10.1021/jp201641h · Source: PubMed

CITATIONS

10

READS

22

4 AUTHORS, INCLUDING:



Carlos Baiz

University of Texas at Austin

40 PUBLICATIONS 409 CITATIONS

SEE PROFILE



Edwin L. Sibert

University of Wisconsin–Madison

103 PUBLICATIONS 2,905 CITATIONS

SEE PROFILE

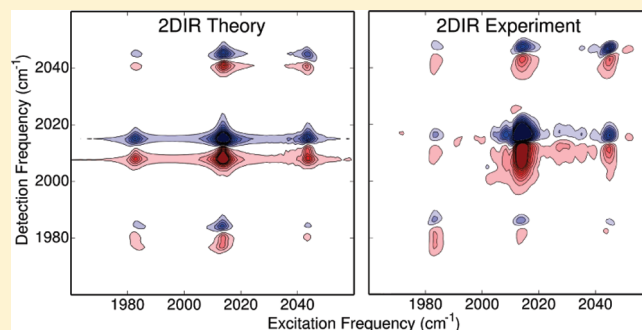
Local-Mode Approach to Modeling Multidimensional Infrared Spectra of Metal Carbonyls

Carlos R. Baiz,^{†,‡} Kevin J. Kubarych,[†] Eitan Geva,[†] and Edwin L. Sibert, III^{*,§}

[†]Department of Chemistry, University of Michigan-Ann Arbor, Ann Arbor, Michigan 48109, United States

[§]Department of Chemistry, University of Wisconsin-Madison, Madison, Wisconsin 53706, United States

ABSTRACT: We present a general approach for modeling multidimensional infrared spectra based on a combination of phenomenological fitting and ab initio electronic structure calculations. The vibrational Hamiltonian is written in terms of bilinearly coupled Morse oscillators that represent local carbonyl stretches. This should be contrasted with the previous approach, where the anharmonic Hamiltonian was given in terms of normal-mode coordinates (Baiz et al. *J. Phys. Chem. A* 2009, 113, 9617). The bilinearly coupled Morse oscillator Hamiltonian is parametrized such that the frequencies and couplings are consistent with experiment, and the anharmonicities are computed by density functional theory. The advantages of the local-mode versus normal-mode approaches are discussed, as well as the ability of different density functionals to provide accurate estimates of the model parameters. The applicability and usefulness of the new approach are demonstrated in the context of the recently measured multidimensional infrared spectra of dimanganese decacarbonyl. The shifts in local site frequencies, couplings, and anharmonicities due to hydrogen bonding to the individual carbonyls are explored. It is found that, even though the effect of hydrogen bonding is nonlocal, it is additive.



I. BACKGROUND

Over the past two decades coherent multidimensional spectroscopy has been established as a powerful probe of the ultrafast dynamics of molecular systems. Two-dimensional infrared (2DIR) spectroscopy, in particular, has provided much insight into the dynamics of systems such as liquid water^{1–3} and peptides.^{4,5} Extracting molecular information from spectra often requires reliable theoretical modeling of the spectral signatures of molecular structure and dynamics. The quality of the supporting model often determines the level of detail and molecular insight that one can obtain.^{6–11}

One commonly used approach for interpreting 2DIR spectra is based on electrostatic maps that link electric fields or electrostatic potentials to frequencies. Usually established by ab initio electronic structure methods, these maps are based on the observation that the vibrational transition frequencies are correlated with the electric field induced on the vibrational mode by the molecular environment.^{6,12,13} Such maps have been successfully employed to interpret the 2DIR spectra in terms of the underlying molecular structure and dynamics in such systems as the amide I stretch in proteins,^{4,14} the OH stretch in liquid water,⁸ and the CN stretch in acetonitrile and thiocyanate.^{9,11}

In this work, we take a first step toward extending the analysis to the case of nonlocal IR probes such as the carbonyl stretches in metal carbonyl complexes. In these cases, one must account for a relatively large number of highly coupled local modes whose

structure and dynamics are best described in terms of an anharmonic excitonic vibrational Hamiltonian.

Metal carbonyl complexes have emerged as useful benchmark systems for nonlinear infrared spectroscopy.^{15–31} Characterized by narrow line shapes, strong infrared activity, complex vibrational structure, and well-defined anharmonic behavior, these complexes have played a central role in facilitating the development of 2DIR spectroscopy, providing insightful demonstrations of the unique ability of 2DIR spectroscopy to resolve vibrational structure and dynamics in multimode systems in liquid solution. The narrow line shapes, stemming from long-lived coherences and populations, also turned metal carbonyls into excellent model systems for exploring coherence–coherence and coherence–population couplings, intramolecular vibrational redistribution, and population relaxation.^{32,33} More recently, metal carbonyls have been employed as nonlocal probes to elucidate how carbonyl–hydroxyl hydrogen bonds partially localize the otherwise delocalized CO stretching modes in $\text{Mn}_2(\text{CO})_{10}$.³⁴

From a theoretical perspective, any attempt to model the 2DIR spectra of metal carbonyls must start with the *anharmonic* vibrational Hamiltonian. A common approach is to model the potential near the (ground-electronic-state) equilibrium

Received: February 18, 2011

Revised: April 16, 2011

Published: May 05, 2011

geometry in terms of a polynomial expansion along the normal-mode coordinates $q = (q_1, q_2, \dots, q_{3N-6})$

$$H = \sum_i \Phi_{ii}(p_i^2 + q_i^2) + \sum_{ijk} \Phi_{ijk} q_i q_j q_k + \sum_{ijkl} \Phi_{ijkl} q_i q_j q_k q_l + \dots \quad (1)$$

Here, the coefficients $\{\Phi_{ijk}\}$ and $\{\Phi_{ijkl}\}$ can be obtained either from electronic structure theory or by fitting to experiment. For example, Golonzka and co-workers were able to obtain the Hamiltonian corresponding to the two carbonyl stretches of dicarbonyl acetylacetonato rhodium(I) (RDC) by fitting to experiment.¹⁶ A subsequent study by Moran and co-workers later demonstrated that the experimental 2DIR spectra are consistent with a Hamiltonian obtained by density functional theory (DFT).³⁵

Although casting the anharmonic Hamiltonian in terms of the normal-mode coordinates and momenta works well for small systems, it is not scalable for larger ones for the following reasons: (1) The set of anharmonic force constants grows rapidly with the number of oscillators, thereby requiring either fitting or calculating an extremely large number of parameters. (2) Using the eigenstates of the harmonic Hamiltonian as a basis requires use of an extremely large number of basis functions in order to obtain well-converged energy levels. As a result, it becomes impractical to diagonalize the anharmonic Hamiltonian of a system such as $\text{Mn}_2(\text{CO})_{10}$ that has ≥ 10 coupled modes.²⁴

In this work, we consider an alternative approach that minimizes the number of free parameters and the size of the basis. To this end, we write the Hamiltonian in terms of the local carbonyl stretch coordinates and momenta, whose local dynamics are described in terms of a Morse potential and are assumed to be bilinearly coupled (see eqs 2 and 3 below). Furthermore, the straightforward physical interpretation of the parameters also makes it easier to either fit them to experiment or calculate them in an ab initio manner. It should be noted that, at least in principle, the local-mode and normal-mode representations of the anharmonic Hamiltonian contain the same information. However, in many cases, the local-mode approach allows for a more intuitive molecular interpretation and is easier to embedded within molecular dynamics (MD) simulations, turning each oscillator into a local probe of its chemical environment, as discussed below.

The rest of this article is organized as follows: In section II, we describe the vibrational Hamiltonian in the local-mode representation and the electronic structure methods used to compute the underlying parameters and demonstrate the applicability of the resulting approach in the case of RDC (see Figure 1). In section III, we describe a hybrid approach that combines ab initio and empirical inputs to obtain the anharmonic vibrational Hamiltonian of the carbonyl stretches in $\text{Mn}_2(\text{CO})_{10}$ and proceed to diagonalize it to obtain the corresponding transition frequencies and dipole moments, as well as the spectra to which they give rise. It should be noted that a similar calculation would have been prohibitively expensive if the Hamiltonian had been cast in terms of normal-mode coordinates and the corresponding harmonic Hamiltonian basis set had been used. We also compare the results between four electronic structure methods and the experimental fit. Excellent agreement is obtained between calculated and experimental 2DIR spectra. In section IV, we explore solvent effects by computing the effect of hydrogen bonding between one of the carbonyls and a methanol molecule. The main results are summarized and their significance pointed out in section V.

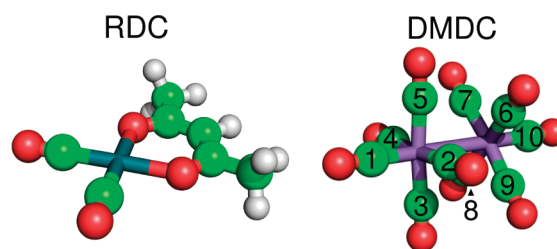


Figure 1. (Left) Equilibrium structures of rhodium(I) dicarbonyl acetylacetonato (RDC) and (right) dimanganese decacarbonyl (DMDC).

II. RDC: LOCAL MODES AND ANHARMONIC POTENTIAL ENERGY SURFACE

Consider a system consisting of N bilinearly coupled Morse oscillators whose Hamiltonian can be written in the form^{36,37}

$$H = \sum_{i=1}^N H_i^0 + \sum_{i>j} H_{ij} \quad (2)$$

Here

$$H_i^0 = \frac{G_{ii}}{2} p_i^2 + D_i (1 - e^{-\alpha_i r_i})^2 \quad (3)$$

where G_{ii} is the inverse reduced mass of each of the oscillators, which correspond to the local CO stretches in a molecule such as DMDC; D_i is the well-depth; α_i is the Morse parameter related to width of the potential; r_i is the vibrational coordinate; and p_i is the corresponding conjugate momentum. The coupling between the local CO stretches is assumed to be given by

$$H_{ij} = G_{ij} p_i p_j + F_{ij} r_i r_j \quad (4)$$

where $\{G_{ij}\}$ and $\{F_{ij}\}$ are yet-to-be-determined coupling coefficients.

In the next step, we express the Hamiltonian in terms of raising and lowering operators

$$H/hc = \sum_i \left[\omega_i \left(\hat{n}_i + \frac{1}{2} \right) - x_{ii} \left(\hat{n}_i + \frac{1}{2} \right)^2 \right] + \sum_{i \neq j}^N \lambda_{ij} (a_i^\dagger a_j + a_i a_j^\dagger) \quad (5)$$

where $\{a_i\}$ and $\{a_i^\dagger\}$ are the lowering and raising operators, respectively; $\hat{n}_i = a_i^\dagger a_i$ are the corresponding number operators; $\omega_i = (2D_i \alpha_i^2 G_{ii})^{1/2} / 2\pi c$ is the local-mode harmonic frequency; $x_{ii} = \hbar c \omega_i^2 / 4D_i$ is the local-mode anharmonicity; and

$$\lambda_{ij} = \sqrt{\omega_i \omega_j} \left(\frac{F_{ij}}{2\sqrt{D_i D_j} \alpha_i \alpha_j} - \frac{G_{ij}}{G_{ii}} \right) \quad (6)$$

represents the coupling coefficients. Importantly, two assumptions have been made in deriving eq 5: (1) The lowering and raising operators ($\{a_i\}$ and $\{a_i^\dagger\}$, respectively) are defined as they would be for the harmonic oscillator rather than the Morse oscillator. (2) Off-resonance coupling terms of the form $(a_i^\dagger a_j^\dagger + a_i a_j)$ are neglected.

It should be noted that, in the case of CO stretches in a system such as DMDC, the frequencies, $\{\omega_i\}$, and coupling constants, $\{\lambda_{ij}\}$, can be extracted from the 2DIR spectra and depend on the

molecular geometry and environment.^{38–42} However, in this work, we attempt to calculate these parameters using DFT in order to shed light on the nature of the couplings in metal carbonyls. Such calculations were carried out on RDC and DMDC (see Figure 1). In the case of RDC, we used the Becke–Perdew exchange–correlation functional (BP86)^{43,44} with a standard LanL2DZ effective core potential⁴⁵ on Rh and the 6-31G(d) basis set on the remaining atoms. In the case of DMDC, we also tested the performance of the BP86 functional against the well-known Becke three-parameter and Lee–Yang–Parr exchange correlation functionals (B3LYP),^{46,47} as well as the use of effective core potential, versus the all-electron 6-31G(d) basis sets on the metal atoms.

RDC contains two identical carbonyls (see Figure 1). The Hamiltonian in eq 5 therefore takes on a particularly simple form in this case. A Hamiltonian of this form was recently parametrized for RDC by Mathew et al.²⁸ by fitting states with up to six excitations. A similar model based on bilinearly coupled cubic local-mode oscillators was also previously parametrized for RDC by Golonzka et al.¹⁶

In this relatively simple case, it can be shown that the fundamental transition frequencies are given by

$$E_{\pm} = \omega_i - 2x_{ii} \pm 2\lambda_{12} \quad (7)$$

The single coupling coefficient, λ_{12} , can therefore be readily extracted from the splitting between the spectral lines that correspond to the asymmetric and symmetric CO stretch fundamental transitions. The frequencies of these transitions have been measured experimentally to be 2014.8 and 2083.2 cm^{−1}, respectively,^{16,28} leading to a value for the coupling coefficient of $\lambda_{12} = 34.2$ cm^{−1}.

The experimental value of the coupling coefficient λ_{12} is found to be in excellent agreement with the difference between the two *normal-mode* frequencies (2000.2 and 2063.3 cm^{−1}) as calculated by a BP86/LanL2DZ/6-31(G) DFT calculation, which is given by $\lambda_{12} = 31.6$ cm^{−1}. Importantly, these *normal-mode* frequencies were obtained by diagonalizing the Hessian matrix of the molecule as a whole, as obtained from DFT.

An alternative method of calculating λ_{12} is from the force constant F_{12} (see eq 6). To this end, we also calculated the internal force constants following the procedure described in the Appendix. Using the value of F_{12} calculated in this manner, we obtained $\lambda_{12} = 12.9$ cm^{−1}, which clearly underestimates the experimental value of λ_{12} .

We were able to trace back the origin for the above-mentioned discrepancy to the failure to account for the contribution of the Rh–C stretch to the “local” carbonyl stretch modes. To this end, we solved for the normal modes of the Rh–C and C–O bonds by diagonalizing the appropriate two-dimensional FG matrix,⁴⁸ where the matrices **G** and **F** were given by (mass units are amu, and force constants are aJ/Å²)

$$\mathbf{G} = \begin{pmatrix} \frac{1}{m_{\text{Rh}}} + \frac{1}{m_{\text{C}}} & -\frac{1}{m_{\text{C}}} \\ -\frac{1}{m_{\text{C}}} & \frac{1}{m_{\text{C}}} + \frac{1}{m_{\text{O}}} \end{pmatrix} = \begin{pmatrix} 0.093 & -0.083 \\ -0.083 & 0.146 \end{pmatrix} \quad \mathbf{F} = \begin{pmatrix} 3.41 & 0.70 \\ 0.70 & 16.33 \end{pmatrix} \quad (8)$$

It should be noted that the relatively large kinetic coupling between the C–O and Rh–C modes does not allow one to

treat the coupling as a small perturbation and that its effect therefore cannot be taken into account using perturbation theory (not shown).

Diagonalization of the FG matrix yields the transformation to a new set of local-mode coordinates

$$\begin{pmatrix} Q_{\text{RhC}} \\ Q_{\text{CO}} \end{pmatrix} = \begin{pmatrix} 4.69 & 2.79 \\ -0.21 & 2.50 \end{pmatrix} \cdot \begin{pmatrix} r_{\text{RhC}} \\ r_{\text{CO}} \end{pmatrix} \quad (9)$$

Assuming that the local modes in eq 2 correspond to the dressed CO stretches as defined in eq 9, we find a value of the coupling coefficient $\lambda_{12} = 30.1$ cm^{−1}, which is clearly in good agreement with the values obtained from experiment and normal-mode analysis.

The strong coupling between the C–O and Rh–C stretches can be explained by the fact that the above transformation is very similar to the following transformation to mass-weighted Jacobi coordinates

$$\begin{pmatrix} R \\ r \end{pmatrix} = \begin{pmatrix} \sqrt{m_{\text{R}}} & \frac{\sqrt{m_{\text{R}}m_{\text{O}}}}{m_{\text{O}} + m_{\text{C}}} \\ 0 & \sqrt{m_{\text{r}}} \end{pmatrix} \cdot \begin{pmatrix} r_{\text{RhC}} \\ r_{\text{CO}} \end{pmatrix} = \begin{pmatrix} 4.69 & 2.67 \\ 0 & 2.62 \end{pmatrix} \cdot \begin{pmatrix} r_{\text{RhC}} \\ r_{\text{CO}} \end{pmatrix} \quad (10)$$

Here, m_{r} is the reduced mass of the CO stretch, and m_{R} is the reduced mass of $m_{\text{C}} + m_{\text{O}}$ and m_{Rh} . Thus, as for the Jacobi coordinates, extending the dressed CO stretch coordinate, Q_{CO} , corresponds to extending r_{CO} while contracting the Rh–C bond. This contraction is significant, as the two Rh–C stretches are adjacent and, hence, directly coupled through the Rh atom. This interpretation of the coupling is consistent with that discussed in Golonzka et al. and attributed to $d_{\pi}-\pi^*$ interactions.¹⁶

To obtain further insight into the vibrational structure of RDC, we computed the full potential energy surface (PES) along the two local CO stretching coordinates. A total of 11 single-point energy calculations for each coordinate were carried out using the BP86 density functional with an effective core potential on Rh as described above. The carbon and oxygen atoms for each carbonyl were displaced along the bond vector while keeping the CO center of mass fixed (eq 9). The resulting potential energy surface (PES) was then fit to a double-Morse potential function with bilinear coupling (see Figure 2)

$$E(r_i, r_j) = D_{\text{O}}[(1 - e^{-\alpha r_i})^2 + (1 - e^{-\alpha r_j})^2] + F_{ij}r_i r_j \quad (11)$$

with $D_{\text{O}} = 1.807$ aJ, $\alpha = 2.301$ Å^{−1}, and $F_{ij} = 0.343$ aJ/Å². This parametric form was found to provide an excellent fit to the PES, as evidenced by a fit coefficient of determination (R^2) value of 0.998.

A CO frequency of 2043 cm^{−1}, an anharmonicity of $X_{ii} = 11.47$ cm^{−1}, and a coupling constant $F_{ij} = 30$ cm^{−1} were obtained from the fit values. These values can be compared directly with the results from the harmonic calculations described above. The CO stretching frequency is in good agreement with the experimental frequency of 2048 cm^{−1} and somewhat higher than the DFT harmonic frequency of 2030 cm^{−1}. The coupling constant F_{ij} compares well with the value of 31.6 cm^{−1} from the harmonic analysis, but it is somewhat lower than the experimental value of 34.2 cm^{−1}. The anharmonicity obtained from the fit is in excellent agreement with the experimental value of 12.1 cm^{−1}. The fit results

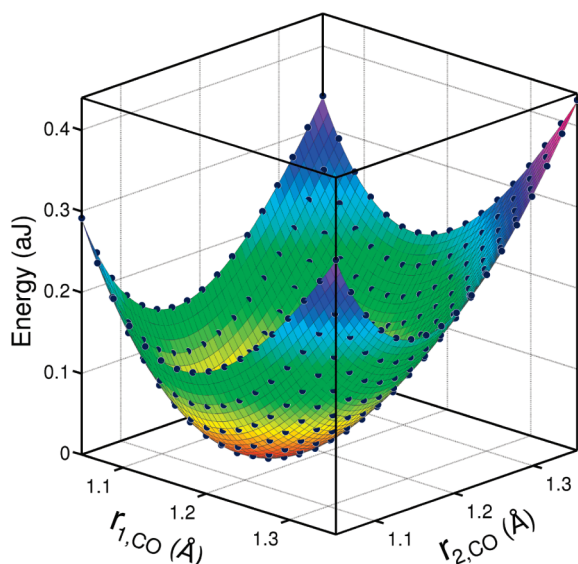


Figure 2. Potential energy surface of RDC along the CO stretching coordinates. The points represent the DFT single-point energies, and the surface is the best fit to the double Morse potential with bilinear coupling (eq 11).

are dependent on the number of fitting parameters used in the model, and one must therefore carefully explore the function space to ensure the reliability of the method. Table 1 lists the results of fitting the PES to a Morse potential with (a) no coupling, (b) bilinear coupling, (c) bilinear and cubic coupling, or (d) bilinear and biquadratic coupling. One observes that the force constant is significantly underestimated if the coupling is neglected and that adding cubic and biquadratic coupling raises the bilinear coupling strength while leaving the site energies unchanged. This might be the origin of the discrepancy between the experimental and fitted bilinear couplings. The RMSE values also show that including the higher-order terms greatly improves the quality of the fit.

For the sake of comparison, we also fitted the PES to a polynomial expansion of up to fourth order

$$E(r_i, r_j) = \Phi_1(r_i^2 + r_j^2) + \Phi_2(r_i^3 + r_j^3) + \Phi_3(r_i^4 + r_j^4) + F_{ij}(r_i r_j) + F_{ij(i+j)}[r_i r_j(r_i + r_j)] + F_{ijij}(r_i^2 r_j^2) \quad (12)$$

The fit parameters are included in Table 1. Compared to the Morse potential, the polynomial model requires additional parameters to converge the fit. Fourth-order diagonal terms are needed to converge the second-order force constant. The second-order force constants obtained from the polynomial fits are also in good agreement with those calculated from the Morse fit, as well as the experimental results. When including second- and third-order force constants and bilinear coupling, a model that contains the same number of fitting parameters as the Morse fit of eq 11, the obtained second-order force constant (8.700 aJ/Å²) is in good agreement with the experimental value (8.683 aJ/Å²). Similarly to the Morse fits, it is important to include as many higher-order terms as required to converge the lower-order parameters. For example, third- and fourth-order terms are needed to converge the second-order force constant. In the Morse and polynomial cases, the effects of the cubic coupling term $F_{ij(i+j)}$ on the lower-order coefficients are

Table 1. RDC Potential Energy Surface Fits along the r_{CO} Coordinate^a

diagonal			off-diagonal			RMSE
Φ_1 calcd	D_{O}	α	F_{ij}	$F_{ij(i+j)}$	F_{ijij}	
r_{CO} Morse Fit						
8.394	2.051	2.232	—	—	—	225.4
8.431	1.807	2.301	0.343	—	—	28.5
8.432	1.804	2.162	0.488	0.0416	—	28.4
8.415	1.797	2.164	0.484	—	1.918	26.3
Φ_1	Φ_2	Φ_3	F_{ij}	$F_{ij(i+j)}$	F_{ijij}	
Polynomial Fit						
8.638	−15.50	—	—	—	—	1317
8.700	−16.40	—	0.441	—	—	151.8
8.408	−18.81	23.96	0.507	—	—	10.6
8.407	−18.84	24.01	0.493	0.0659	—	10.0
8.407	−18.79	23.74	0.503	—	0.7178	10.0
Experimental Fit						
8.683	—	—	0.472	—	—	—
Harmonic Hessian Analysis						
8.328	—	—	0.4030	—	—	—
^a Force constants are in units of aJ and Å; root mean square errors (RMSEs) are in cm ^{−1} .						

^aForce constants are in units of aJ and Å; root mean square errors (RMSEs) are in cm^{−1}.

very similar to those of the quartic (bilinear) term F_{ijij} . The RMSE values also show that the Morse equation with bilinear coupling gives a significantly better fit than the equivalent polynomial fit.

III. DMDC: LOCAL MODES AND ANHARMONIC POTENTIAL ENERGY SURFACE

Having verified our approach for RDC, we now turn our attention to DMDC, which is our primary interest. The structure of DMDC, along with the numbering scheme of the sites, is shown in Figure 1. The force constant matrix takes the form

$$F = \begin{pmatrix} S_1 & C_1 & C_1 & C_1 & C_1 & C_2 & C_2 & C_2 & C_2 & C_3 \\ C_1 & S_2 & C_4 & C_5 & C_4 & C_6 & C_7 & C_7 & C_6 & C_2 \\ C_1 & C_4 & S_2 & C_4 & C_5 & C_6 & C_6 & C_7 & C_7 & C_2 \\ C_1 & C_5 & C_4 & S_2 & C_4 & C_7 & C_6 & C_6 & C_7 & C_2 \\ C_1 & C_4 & C_5 & C_4 & S_2 & C_7 & C_7 & C_6 & C_6 & C_2 \\ C_2 & C_6 & C_6 & C_7 & C_7 & S_2 & C_4 & C_5 & C_4 & C_1 \\ C_2 & C_7 & C_6 & C_6 & C_7 & C_4 & S_2 & C_4 & C_5 & C_1 \\ C_2 & C_7 & C_7 & C_7 & C_6 & C_5 & C_4 & S_2 & C_4 & C_1 \\ C_2 & C_6 & C_7 & C_7 & C_6 & C_4 & C_5 & C_4 & S_2 & C_1 \\ C_3 & C_2 & C_2 & C_2 & C_2 & C_1 & C_1 & C_1 & C_1 & S_1 \end{pmatrix} \quad (13)$$

where S_1 and S_2 correspond to the axial and equatorial carbonyls respectively. The coupling elements C_1 – C_7 represent the seven different coupling interactions between the carbonyls.

Similarly to RDC, we find that the Mn–C stretch makes a significant contribution to the local CO modes

$$\begin{pmatrix} Q_{\text{MnC}} \\ Q_{\text{CO}} \end{pmatrix} = \begin{pmatrix} 4.30 & 2.57 \\ -0.18 & 2.51 \end{pmatrix} \cdot \begin{pmatrix} r_{\text{MnC}} \\ r_{\text{CO}} \end{pmatrix} \quad (14)$$

As for RDC, this transformation turns out to be similar to the transformation to mass-weighted Jacobi coordinates

$$\begin{pmatrix} R \\ r \end{pmatrix} = \begin{pmatrix} 4.31 & 2.46 \\ 0 & 2.62 \end{pmatrix} \cdot \begin{pmatrix} r_{\text{MnC}} \\ r_{\text{CO}} \end{pmatrix} \quad (15)$$

The local CO force constants for DMDC can be obtained from electronic structure calculations by projecting the Hessian from Cartesian coordinates onto the local CO stretch coordinates. We computed the Hessian by DFT using both the BP86 and B3LYP functionals. We also tested the reliability of using the LanL2DZ effective core potential on the Mn atoms by comparing the results to those obtained with an all-electron basis set. Table 2 reports the site energies and couplings obtained by fitting to experiment and computed by using the different functionals and basis sets. The fit was performed using a genetic algorithm that involves independently varying each of the nine parameters (two site energies and seven coupling constants) while minimizing the mean square deviations between the fit and experimental frequencies and transition dipoles. It is important to note that the fit minimum is well constrained but not unique: the site energies and couplings can vary over a small range while yielding essentially the same frequencies and transition dipoles.

Table 2 shows that the computed results are in reasonable agreement with experiment. BP86 is seen to somewhat underestimate the site energies, S_1 and S_2 , compared to experiment, whereas B3LYP overestimates them by a similar amount. The two functionals predict similar values of the coupling coefficients, C_1 – C_7 , which are all in reasonable agreement with experiment. It should be noted, however, that the relative errors in the smaller coupling coefficients might be due to the inability of these functionals to account for long-range interactions such as the through-space interactions between carbonyls.⁴⁹ Table 2 also shows that effective core potentials do not have a significant effect on the CO frequencies. This is not surprising given that the basis sets on the carbon and oxygen atoms remain the same and the electronic structure of the metal centers plays a relatively minor role in determining the through-bond coupling strengths.

Local anharmonicities (x_{ii}) of the axial and equatorial carbonyls can be obtained by displacing the C and O atoms along the local-mode coordinate and fitting the resulting potential to a Morse function. Figure 3 shows the potential energy surfaces for the axial and equatorial carbonyls, along with the respective Morse fits, and the fit parameters are listed in Table 3. Once the anharmonicities are known, it is straightforward to construct a bilinearly coupled Morse Hamiltonian (eq 2). In what follows we use the experimentally fitted site energies and coupling constants (Table 2, rightmost column) along with the anharmonicities extracted from the Morse fit (Table 3). To overcome any possible ambiguity in assigning overtones and combination bands, we used a correlation plot that relates the energy levels of the anharmonic Hamiltonian with the corresponding values for the harmonic ones. Starting with the harmonic Hamiltonian ($x_{ii} = 0$), the anharmonicity is increased while following the energy levels from the harmonic to the final anharmonic values (see Figure 4). Each eigenstate can be labeled as either an

Table 2. Quadratic Force Constants for DMDC Calculated at Different Levels of Electronic Structure Theory

	BP86	BP86 ^a	B3LYP	B3LYP ^a	fit
S_1	2008.27	2001.53	2088.63	2083.26	2046.97
S_2	2013.73	2009.00	2092.52	2088.75	2038.01
C_1	15.60	15.78	14.15	14.58	20.80
C_2	3.03	2.80	4.99	4.64	5.88
C_3	4.05	4.09	5.30	5.16	5.17
C_4	10.62	10.85	9.53	9.81	5.26
C_5	20.28	20.96	15.04	15.89	18.51
C_6	13.88	13.59	16.63	16.37	15.29
C_7	2.54	2.26	4.81	4.49	3.62

^a No effective core potentials.

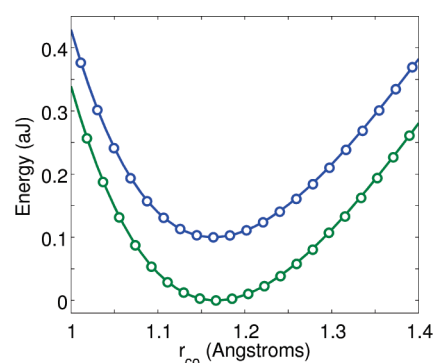


Figure 3. Potential energy surface along the (top) axial and (bottom) equatorial CO stretching coordinates of DMDC calculated with a BP86 density functional and effective core potential on the Mn atoms. The circles represent the computed single-point energies, and solid lines are the Morse fits as described in the text. The plots are vertically offset for clarity.

Table 3. Morse Fits of the DMDC PES along the Axial and Equatorial CO Coordinates Shown in Figure 3

	D_i (aJ)	α_i (\AA^{-1})	ω_i (cm^{-1})	x_{ii} (cm^{-1})
axial CO	1.678	2.237	2038.9	12.3
equatorial CO	1.770	2.176	2037.9	11.6

overtone or a combination band. Ambiguities arise in the case of degenerate states, in which case the transition dipole vectors can serve to evaluate the contributions from each one-quantum state.

The calculated normal-mode anharmonicities ($\Delta = \omega_{01} - \omega_{12}$) are listed in Table 4, along with the experimental results for the infrared-active modes of DMDC. For comparison, we include previous results from ref 23 obtained using second-order vibrational perturbation theory (VPT2)^{50,51} with the same DFT procedure (BP86/LanL2DZ/6-31G(d)). Qualitative agreement between the local CO Hamiltonian, VPT2, and experiment show how, by exploiting the high degree of symmetry in DMDC, one can compute anharmonic frequencies at relatively low computational cost while keeping the number of fitting parameters tractable and retaining most of the molecular details of interest.

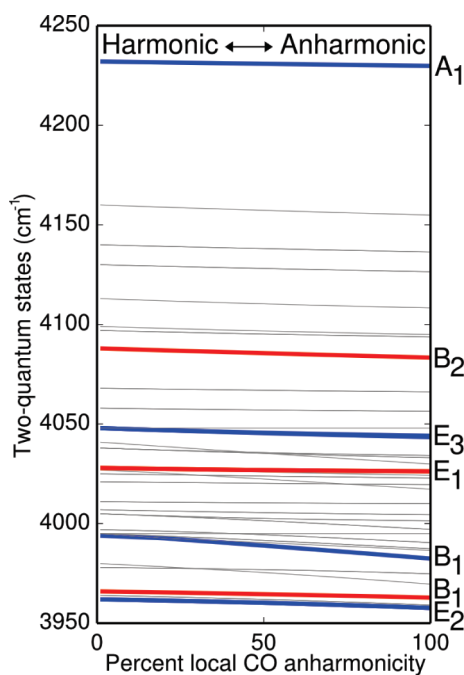


Figure 4. Normal-mode correlation plot for the two-quanta states of DMDC. The IR-active and IR-inactive overtone states are shown in red and blue, respectively. The symmetry of each state's mode is shown on the right. The gray lines correspond to combination states.

Table 4. Normal-Mode Frequencies and Overtone Anharmonicities of DMDC Obtained from the Local Carbonyl Stretching Hamiltonian along with the Experimental Values^{23 a}

mode	exptl	fit	calcd anharm	VPT2	exptl
1	1981 ^b	1981.0	4.4	4.3	
2	1981 ^b	1981.0	4.4	4.3	
3	1983 ^c	1983.0	3.2	5.4	8.3
4	1997 ^b	1997.0	7.4	8.0	
5	2014 ^c	2014.0	1.8	4.5	6.5
6	2014 ^c	2014.0	1.8	4.5	6.5
7	2024 ^b	2024.0	3.0	3.0	
8	2024 ^b	2024.0	3.9	3.0	
9	2044 ^b	2044.0	4.6	3.5	4.4
10	2116 ^b	2116.0	2.2	2.6	

^a Second-order vibrational perturbation theory (VPT2) anharmonicities from ref 23 included for comparison. ^b Raman spectra in nonpolar solvents. ^c IR absorption and transient absorption in cyclohexane.

It is important to discuss the limitations of the current modeling framework and its applicability to larger, less-symmetric systems. The analytical ab initio calculation of the Hessian will become an important challenge as the system size increases. However, working in the center-of-mass coordinates, the full quadratic force field can be calculated by finite differentiation in the reduced N -dimensional subspace of the local modes of interest, and so, there is a maximum of $N(N + 1)/2$ unique elements in the F matrix, assuming no symmetry. The key role of symmetry is to greatly reduce the number of independent F -matrix elements. Phenomenological fitting of the F -matrix

elements will become significantly more challenging in less-symmetric systems because the fits are less likely to be unique.

Two-Dimensional Spectroscopy. Two-dimensional infrared spectra are directly related to the third-order nonlinear response function of the system $S^{(3)}(t_1, t_2, t_3)$, which contains information on the one- and two-quanta energy levels, anharmonic couplings, and vibrational dynamics. The measured spectra can be expressed as a convolution of the response function with the applied laser fields $[E_1(t), E_2(t), E_3(t)]$. The analytical ab initio calculation of the Hessian becomes a significant challenge as the system size increases. However, working in the center-of-mass coordinates, the full quadratic force field can be calculated by finite differentiation in the reduced N -dimensional subspace of the local modes of interest, and so, there is a maximum of $N(N + 1)/2$ unique elements in the F matrix assuming no symmetry. The important role of symmetry is to greatly reduce the number of independent F -matrix elements. Phenomenological fitting of the F -matrix elements is significantly more challenging in less-symmetric systems because the fits are less likely to be unique.

$$P^{(3)}(t) = \int_0^\infty dt_1 \int_0^\infty dt_2 \int_0^\infty dt_3 S^{(3)}(t_1, t_2, t_3) E_1(t - t_3) E_2(t - t_3 - t_2) E_3(t - t_3 - t_2 - t_1) \quad (16)$$

Here, the response functions of DMDC were calculated within the framework of Redfield theory.⁵² The phenomenological rate constants for dephasing, intramolecular vibrational redistribution (IVR), and population relaxation were set to their empirical values of 3, 4, and 50 ps⁻¹, respectively. Anharmonic frequencies extracted from the local CO Hamiltonian (eq 2), along with the Harmonic transition dipole moments (BP86), were used to construct the molecular Hamiltonian in the normal-mode representation. The laser pulse interactions were treated as impulsive on the time scale of vibrational relaxation.

Figure 5 shows simulated and experimental 2DIR spectra of DMDC. The experimental spectrum was collected using a Fourier transform 2DIR spectrometer as described in detail elsewhere.²⁹ For comparison, Figure 6 shows projections of 2DIR spectra onto the detection axis. Such projections are equivalent to measuring the dispersed transient absorption signal. The 2DIR spectrum features three main diagonal peaks and the corresponding cross-peaks. The negative (blue) ground-state bleach peaks appear at the frequencies corresponding to the $0 \rightarrow 1$ transitions, whereas the positive (red) excited-state absorption features are due to transitions between the one- and two-quanta states ($1 \rightarrow 2$) and are referred to as “anharmonic” peaks. The splitting between a negative peak and its corresponding positive peak is given by the anharmonicity of overtones (diagonal peaks) and combination bands (off-diagonal peaks): $\Delta = \omega_{01} - \omega_{12}$. The center frequencies, intensities, and line shapes in the calculated spectrum are in good agreement with the experimental spectrum. It is important to note that the amplitude of the two-dimensional peaks is dictated by two different factors: (1) the orientationally averaged transition dipole moment, in analogy to linear absorption spectroscopy, and (2) the overlap between negative (ground-state bleach) and positive (excited-state absorption) peaks, which is given by the anharmonicities and line widths of the peaks. To illustrate this effect, consider a harmonic oscillator. In this case, the frequency of the $0 \rightarrow 1$ transition is the same as that of the $1 \rightarrow 2$ transition, and therefore, positive and negative contributions appear at the

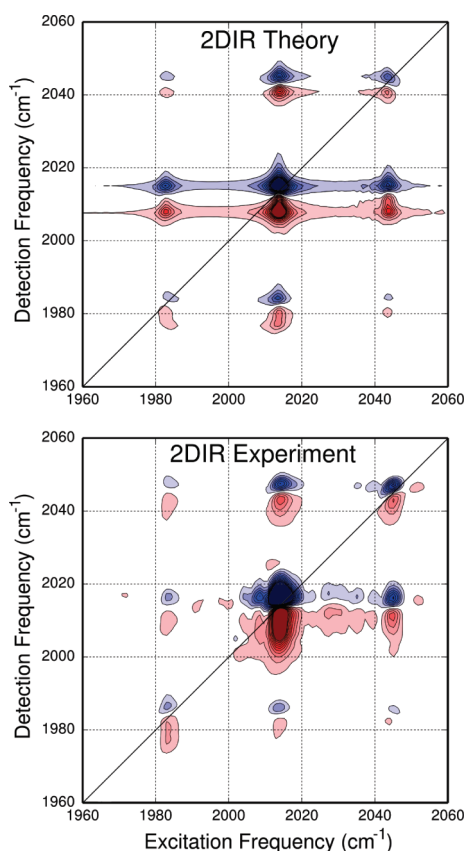


Figure 5. Simulated and experimental absorptive two-dimensional infrared spectra of DMDC at a waiting time of 5 ps. The experimental spectrum was collected in *n*-hexane, a weakly interacting solvent.

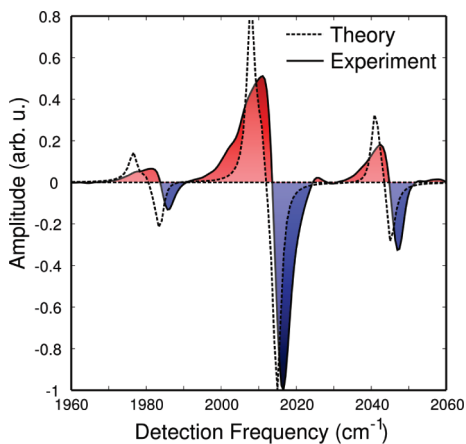


Figure 6. Projection of the 2DIR spectrum (Figure 5) onto the detection axis.

same frequency. Because the two peaks have the same intensity, the two contributions should effectively cancel out. Although the calculated anharmonicities are smaller than the experimentally measured values, the peaks are sufficiently narrow and well-separated that the amplitude is not significantly affected by the overlap.

In the experimental spectrum of DMDC, the anharmonic peaks are broader than the ground-state bleaches, showing that

the second-quanta energy levels are affected to a greater extent by the solvent fluctuations. This effect is not captured by the simulations, as the dephasing times (peak widths) of ground- and excited-state transitions are equal. However, it is worth pointing out that these effects are naturally captured when frequency fluctuations are computed from molecular dynamics simulations.³³ One additional observation worth discussing in this context is the spectroscopic effect of the 1% natural ¹³C isotope abundance. In the case of DMDC, about 10% of the molecules contain at least one substituted ¹³CO ligand. If the substitution occurs on an axial CO, a new peak centered near 2002 cm⁻¹ appears in the spectrum, whereas an equatorial substitution will give rise to new peaks at 1950 and 1956 cm⁻¹.²³ The new peak near 2002 cm⁻¹ is seen in the experimental absorption and 2DIR spectra. It is straightforward to simulate this effect using the local CO Hamiltonian, but because of the highly delocalized nature of the CO vibrations, this is significantly more challenging when working in the normal-mode representation.

IV. HYDROGEN BONDING

The theoretical framework described in the previous section relies on gas-phase electronic structure calculations and the assumption of weak coupling with the solvent. In this section, we consider the effects of interaction with a strongly coupled hydrogen-bonded solvent such as methanol. In this case, hydrogen bonds can form between the solvent OH groups and the CO groups in RDC and DMDC. Recent 2DIR studies of DMDC in hydrogen-bonding solvents have suggested that DMDC can be used as a nonlocal probe of the hydrogen-bonded network. Hydrogen bonds formed between carbonyls and the solvent give rise to frequency fluctuations of the local sites and, correspondingly, the normal modes. Two-dimensional infrared spectroscopy essentially measures these correlations by mapping the joint transition frequencies between pairs of eigenstates. In the case of a strongly coupled set of oscillators, such as in DMDC, normal modes are highly delocalized, with each CO site contributing to a large number of normal modes. Consequently, a single hydrogen bond will shift the frequencies of many normal modes. In contrast, the local CO frequencies should be mostly sensitive to the local environment around each ligand; thus, decomposing the normal-mode frequency fluctuations into linear combinations of local-mode fluctuations will offer a more intuitive molecular perspective of the solvation dynamics in hydrogen-bonding liquids. For example, consider a single solvent molecule switching hydrogen bonds between two adjacent CO sites; this scenario would lead to the two local frequencies being anticorrelated. Measuring the local-site correlation thus turns a molecule such as DMDC into a molecular probe of the liquid dynamics, where each site behaves as an individual reporter of the local environment fluctuations, but the molecule as a whole has the ability to probe longer-range delocalized fluctuations of the solvent. In this section, we explore the effects of hydrogen bonding on the carbonyl frequencies by constructing a set of model systems consisting of RDC and DMDC with methanol molecules σ -hydrogen-bonded to the carbonyl groups. We test the effects of a single hydrogen bond as well as two hydrogen bonds to adjacent carbonyl groups.

A. RDC. In the case of RDC, the two carbonyls are equivalent. The geometry of the complex was optimized using the BP86 functional with an effective core potential on the metal atoms. No

Table 5. Local CO Frequencies and Anharmonicities of RDC with a Single Hydrogen Bond (HB) to a CO Group As Well As Two Hydrogen Bonds to Each CO Group

CO site	D_i (aJ)	α_i (\AA^{-1})	ω_i (cm^{-1})	x_{ii} (cm^{-1})
One HB				
1 (HB)	1.811	2.147	2032.9	11.3
2	1.812	2.162	2047.7	11.5
coupling			30.6	
Two HB				
1 (HB)	1.805	2.152	2035.4	11.4
2 (HB)	1.805	2.152	2035.4	11.4
coupling			31.5	

geometric constraints were placed on the optimization. The force field parameters were obtained by finite displacements along the CO coordinates and fit to a bilinearly coupled Morse potential as described above. Table 5 reports the two frequencies and anharmonicities corresponding to the hydrogen-bonded and free CO sites. These can be compared directly with the gas-phase values listed in Table 1. The hydrogen-bonded site energy red shifts from 2043.0 to 2032.9 cm^{-1} , whereas the free CO blue shifts from 2043.0 to 2047.7 cm^{-1} . These results suggest that, even though hydrogen-bonding is local, its spectral impact is nonlocal. The through-bond coupling between adjacent sites likely accounts for much of the nonlocal nature of the perturbation. The effect of hydrogen bonding on the bilinear coupling is relatively small, increasing from 30.0 to 30.6 cm^{-1} .

To test whether the hydrogen-bonding effects are additive, we now examine the case of forming two hydrogen bonds to different sites in the molecule. If we take the contributions to be independent, starting from 2043.0 cm^{-1} for the gas-phase case and taking the values for the single hydrogen-bonded case, there should be, first, a lowering by 10.1 cm^{-1} due to the local HB and, second, a raising by 4.7 cm^{-1} due to the HB to the adjacent CO, giving a total frequency of 2037.6 cm^{-1} . This value compares favorably to the doubly hydrogen-bonded case where the frequency is 2035.4 cm^{-1} , suggesting that the contributions are mostly independent. The bilinear coupling shows similar effects: the first HB increases the coupling from 30.0 to 30.6 cm^{-1} , and the second increases it to 31.5 cm^{-1} , showing that, to a good first approximation, the individual HB contributions to the coupling strength can also be treated additively.

B. DMDC. The larger number of sites in DMDC enable us to better evaluate the nonlocal effect of hydrogen bonding and its additivity. Table 6 shows the frequencies and anharmonicities of the four different carbonyl sites when DMDC is hydrogen-bonded with an equatorial carbonyl (site 2, Figure 7). The hydrogen-bonded site red shifts from 2037.9 cm^{-1} (gas phase, Table 3) to a value of 2024.7 cm^{-1} . In addition, all nearby CO site frequencies are also affected by the hydrogen bonding. However, because there is a larger number of carbonyls, the impact per carbonyl is smaller than in RDC. If the strength of the neighbor perturbation is somehow proportional to the coupling strength (Table 2), we would expect the frequency increase of site 4 to be larger than that of site 3. This is, in fact, the case: the frequency of site 3 increases by 1.3 cm^{-1} , and that of site 4 increases by 3.3 cm^{-1} . Surprisingly, the axial carbonyl frequency decreases by 1.2 cm^{-1} , indicating that additional factors affect the frequency shifts of the neighboring sites.

Table 6. Local CO Frequencies and Anharmonicities of DMDC with a Single Hydrogen Bond (HB) to an Equatorial CO Group (The Site Numbers Correspond to the CO Sites Labeled in Figure 7, and the CO Frequencies in the Absence of HBs are Reported in Table 3)

CO site	D_i (aJ)	α_i (\AA^{-1})	ω_i (cm^{-1})	x_{ii} (cm^{-1})
One HB				
1	1.742	2.194	2037.7	11.8
2 (HB)	1.669	2.227	2024.7	12.1
3	1.681	2.236	2039.2	12.3
4	1.687	2.233	2041.2	12.2
Two HB				
1	1.744	2.195	2039.7	11.8
2 (HB)	1.670	2.228	2025.6	12.2
3 (HB)	1.670	2.228	2025.6	12.2
4	1.683	2.238	2043.3	12.3

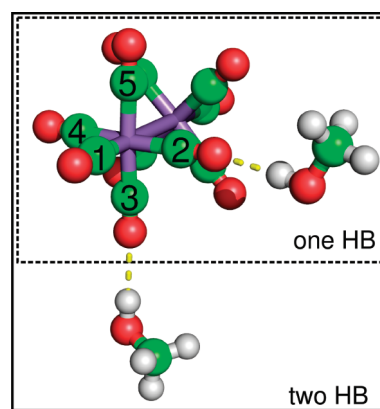
**Figure 7.** Equilibrium structure of the DMDC–methanol complexes used to test the effect of hydrogen bonding.

Table 6 also lists the frequencies of the carbonyls in the case where two adjacent sites are hydrogen-bonded. From the one-HB case, we have a 13.2 cm^{-1} red shift due to hydrogen bonding of the site and a 1.3 cm^{-1} blue shift due to a HB neighbor. Starting from the 2037.9 cm^{-1} frequency of an axial CO in the gas-phase case (Table 3), we expect a final frequency of 2026.0 cm^{-1} . This value is in excellent agreement with the 2025.6 cm^{-1} obtained from the two-HB model. Similarly, adding up the individual contributions to the frequency of site 4 (one perpendicular and one opposite HB carbonyl), we predict a blue shift of 4.6 cm^{-1} , which compares well with the extracted shift of 5.4 cm^{-1} .

The results show that the individual hydrogen-bonding contributions can be treated independently and that the coupling strengths and anharmonicities are unaffected by hydrogen bonding. Therefore, it would be straightforward to develop a parametrized local-mode Hamiltonian to account for the site perturbations due to hydrogen bonding. Such a model can be easily embedded within molecular dynamics simulations to compute the normal-mode frequency fluctuations and the subsequent two-dimensional spectra.

In both metal carbonyls, hydrogen bonding is only a minor perturbation of the overall electronic structure of the molecule. This is reflected by the small changes in site frequencies: only

0.5% of the total frequency. Because the couplings and anharmonicities are approximately 2 orders of magnitude smaller than the site energies, the same 0.5% perturbation of these parameters remains nearly imperceptible compared to the larger site-energy changes. Therefore, solvent effects in metal carbonyls can be described in terms of fluctuations of the local site energies.

V. CONCLUSIONS AND OUTLOOK

We have presented a new hybrid approach for modeling the vibrational structure and dynamics of metal carbonyls and the corresponding two-dimensional spectra that is based on describing the Hamiltonian in terms of bilinearly coupled Morse oscillators. The local site anharmonicities are obtained from electronic structure calculations, whereas the couplings are fit to reproduce the linear IR absorption and Raman spectra. Fitting the frequencies to experiment greatly reduces the computational expense and increases the accuracy of the model. The harmonically coupled Morse Hamiltonian allowed one- and two-quanta anharmonic frequencies to be obtained for a 10-mode system, DMDC, a task that is exceedingly challenging by the normal-mode approach because of its enormous computational requirement. We have demonstrated that the model can successfully reproduce the two-dimensional infrared spectrum of DMDC.

This intuitive local-mode framework provides practical insights into the vibrational structure of the systems that are not easily accessible in the normal-mode representation. We examined the effects of hydrogen bonding on local carbonyl frequencies in RDC and DMDC and found that the perturbations are pronouncedly nonlocal and yet additive. We also found that the coupling constants and anharmonicities are relatively insensitive to hydrogen bonding. These observations pave the way to calculating the frequency fluctuations in multimode systems in strongly interacting solvents, thereby providing an atomistic view of the local and nonlocal fluctuations in the solvation environment surrounding the molecule.

■ APPENDIX

There are many approaches to calculating the internal force constant matrix elements from the Cartesian coordinate Hessian. In this work, we follow Wilson, Decius, and Cross⁴⁸ and write

$$\mathbf{S} = \mathbf{B}\mathbf{x} \quad (17)$$

where we include the center-of-mass and Eckart constraints so that \mathbf{B} is a $3N \times 3N$ matrix. Here, \mathbf{S} represents the matrix of atomic displacements in internal coordinates (e.g., bond stretches), and \mathbf{B} is the matrix that translates Cartesian displacements to internal coordinate displacements. The elements of the \mathbf{B} matrix are defined as the first derivatives

$$B_{ij} = \frac{\partial S_i}{\partial x_j} \quad (18)$$

The first $3N - 6$ rows of the \mathbf{B} matrix are calculated by finite difference by extending a single Cartesian coordinate in the plus and minus directions and determining the corresponding changes in the internal coordinates.

If the first N columns of the \mathbf{B} matrix correspond to differentiation with respect to x and the next N correspond to differentiation with respect to y and so forth, then the coordinates

corresponding the center of mass are

$$\begin{aligned} S_{3N-5} &= \sum_{i=1}^N m_i x_i / m_{\text{total}} \\ S_{3N-4} &= \sum_{i=N+1}^{2N} m_i y_i / m_{\text{total}} \\ S_{3N-3} &= \sum_{i=2N+1}^{3N} m_i z_i / m_{\text{total}} \end{aligned} \quad (19)$$

and $B_{3N-5,i} = m_i / m_{\text{total}}$, where x_i , y_i , and z_i are the Cartesian coordinates; m_i is the mass of the i th atom; and m_{total} is the total mass of the molecule. A similar expression is found for the three rows of the \mathbf{B} matrix corresponding to rotations. For rotation about the x axis, the expression is

$$S_{3N-2} = \sum_{i=1}^N m_i (x_{2N+i} x_{N+i,e} - x_N x_{2N+i,e}) \quad (20)$$

where the subscript e denotes the equilibrium value of the coordinates. As above, the corresponding elements of the \mathbf{B} matrix are obtained by finite differentiation.

Inverting \mathbf{B} gives $\mathbf{x} = \mathbf{B}^{-1}\mathbf{S}$. This leads to a force constant matrix

$$\mathbf{F} = [\mathbf{B}^{-1}]^T \mathbf{V} \mathbf{B}^{-1} \quad (21)$$

where \mathbf{V} is the Hessian in non-mass-weighted Cartesian coordinates.

Any choice of the internal coordinates can be used. For example, the internal coordinates of the standard \mathbf{Z} -matrix input of electronic structure programs are acceptable.

■ AUTHOR INFORMATION

Corresponding Author

*E-mail: sibert@chem.wisc.edu.

Present Addresses

[†]Department of Chemistry, Massachusetts Institute of Technology, Cambridge, Massachusetts 02139, United States.

■ ACKNOWLEDGMENT

C.R.B. acknowledges support from a Predoctoral Fellowship by the Rackham Graduate School at the University of Michigan. E.L.S. acknowledges support by the National Science Foundation under Grant CHE-0911559.

■ REFERENCES

- (1) Cowan, M. L.; Bruner, B. D.; Huse, N.; Dwyer, J. R.; Chugh, B.; Nibbering, E. T. J.; Elsaesser, T.; Miller, R. J. D. *Nature* **2005**, *434*, 199.
- (2) Kraemer, D.; Cowan, M. L.; Paarmann, A.; Huse, N.; Nibbering, E. T. J.; Elsaesser, T.; Miller, R. J. D. *Proc. Natl. Acad. U.S.A.* **2008**, *105*, 437.
- (3) Roberts, S. T.; Ramasesha, K.; Tokmakoff, A. *Acc. Chem. Res.* **2009**, *42*, 1239.
- (4) Smith, A. W.; Lessing, J.; Ganim, Z.; Peng, C. S.; Tokmakoff, A.; Roy, S.; Jansen, T. L. C.; Knoester, J. *J. Phys. Chem. B* **2010**, *114*, 10913.
- (5) Backus, E. H. G.; Bloem, R.; Donaldson, P. M.; Ihalainen, J. A.; Pfister, R.; Paoli, B.; Caflisch, A.; Hamm, P. *J. Phys. Chem. B* **2010**, *114*, 3735.
- (6) Corcelli, S. A.; Lawrence, C. P.; Skinner, J. L. *J. Chem. Phys.* **2004**, *120*, 8107.

- (7) Asbury, J. B.; Steinel, T.; Stromberg, C.; Corcelli, S. A.; Lawrence, C. P.; Skinner, J. L.; Fayer, M. D. *J. Phys. Chem. A* **2004**, *108*, 1107.
- (8) Schmidt, J.; Roberts, S.; Loparo, J.; Tokmakoff, A.; Fayer, M.; Skinner, J. *Chem. Phys.* **2007**, *341*, 143.
- (9) Choi, J. H.; Oh, K. I.; Lee, H.; Lee, C.; Cho, M. *J. Chem. Phys.* **2008**, *128*, 134506.
- (10) Choi, J.-H.; Oh, K.-I.; Cho, M. *J. Chem. Phys.* **2008**, *129*, 174512.
- (11) Oh, K. I.; Choi, J. H.; Lee, J. H.; Han, J. B.; Lee, H.; Cho, M. *J. Chem. Phys.* **2008**, *128*, 154504.
- (12) Jansen, T. I. C.; Knoester, J. *Acc. Chem. Res.* **2009**, *42*, 1405.
- (13) Lee, H.; Choi, J. H.; Cho, M. *Phys. Chem. Chem. Phys.* **2010**, *12*, 12658.
- (14) Ganim, Z.; Jones, K. C.; Tokmakoff, A. *Phys. Chem. Chem. Phys.* **2010**, *12*, 3579.
- (15) Rector, K.; Fayer, M. *Int. Revs. Phys. Chem.* **1998**, *17*, 261.
- (16) Golonzka, O.; Khalil, M.; Demirdoven, N.; Tokmakoff, A. *J. Chem. Phys.* **2001**, *115*, 10814.
- (17) Asbury, J.; Steinel, T.; Fayer, M. *Chem. Phys. Lett.* **2003**, *381*, 139.
- (18) Butler, J.; George, M.; Schoonover, J.; Dattelbaum, D.; Meyer, T. *Coord. Chem. Rev.* **2007**, *251*, 492.
- (19) Strassfeld, D.; Shim, S.; Zanni, M. T. *Phys. Rev. Lett.* **2007**, *99*, 038102.
- (20) Ding, F.; Zanni, M. T. *Chem. Phys.* **2007**, *341*, 95.
- (21) DeFlores, L. P.; Nicodemus, R. A.; Tokmakoff, A. *Opt. Lett.* **2007**, *32*, 2966.
- (22) Cahoon, J. F.; Sawyer, K. R.; Schlegel, J. P.; Harris, C. B. *Science* **2008**, *319*, 1820.
- (23) Baiz, C. R.; McRobbie, P. L.; Preketes, N. K.; Kubarych, K. J.; Geva, E. *J. Phys. Chem. A* **2009**, *113*, 9617.
- (24) Baiz, C. R.; McRobbie, P. L.; Anna, J. M.; Geva, E.; Kubarych, K. J. *Acc. Chem. Res.* **2009**, *42*, 1395.
- (25) Baiz, C. R.; McCanne, R.; Kubarych, K. J. *J. Am. Chem. Soc.* **2009**, *131*, 13590.
- (26) Baiz, C. R.; McCanne, R.; Nee, M. J.; Kubarych, K. J. *J. Phys. Chem. A* **2009**, *113*, 8907.
- (27) Baiz, C. R.; McCanne, R.; Kubarych, K. J. *Appl. Spectrosc.* **2010**, *64*, 3.
- (28) Mathew, N. A.; Yurs, L. A.; Block, S. B.; Pakoulev, A. V.; Kornau, K. M.; Sibert, E. L.; Wright, J. C. *J. Phys. Chem. A* **2010**, *114*, 817.
- (29) Anna, J. M.; Nee, M. J.; Baiz, C. R.; McCanne, R.; Kubarych, K. J. *J. Opt. Soc. Amer. B-Opt. Phys.* **2010**, *27*, 382.
- (30) Ogilvie, J. P.; Kubarych, K. J. *Adv. At. Mo. Opt. Phys.* **2009**, *57*, 249.
- (31) Xiong, W.; Laaser, J. E.; Paoprasert, P.; Franking, R. A.; Hamers, R. J.; Gopalan, P.; Zanni, M. T. *J. Am. Chem. Soc.* **2009**, *131*, 18040.
- (32) Nee, M. J.; Baiz, C. R.; Anna, J. M.; McCanne, R.; Kubarych, K. J. *J. Chem. Phys.* **2008**, *129*, 084503.
- (33) Baiz, C. R.; Kubarych, K. J.; Geva, E. *J. Phys. Chem. B*, published online Mar 4, 2011, <http://dx.doi.org/10.1021/jp109357d>.
- (34) King, J. T.; Baiz, C. R.; Kubarych, K. J. *J. Phys. Chem. A* **2010**, *114*, 10590.
- (35) Moran, A. M.; Dreyer, J.; Mukamel, S. *J. Chem. Phys.* **2003**, *118*, 1347.
- (36) Halonen, L.; Child, M. S.; Carter, S. *Mol. Phys.* **1982**, *47*, 1097.
- (37) Halonen, L.; Child, M. S. *J. Chem. Phys.* **1983**, *79*, 4355.
- (38) Krimm, S.; Bandekar, J. *Adv. Protein Chem.* **1986**, *38*, 181.
- (39) Torii, H. *J. Phys. Chem. B* **2008**, *112*, 8737.
- (40) la Cour Jansen, T.; Dijkstra, A. G.; Watson, T. M.; Hirst, J. D.; Knoester, J. *J. Chem. Phys.* **2006**, *125*, 044312.
- (41) Hamm, P.; Woutersen, S. *Bull. Chem. Soc. Jpn.* **2002**, *75*, 985.
- (42) Krummel, A. T.; Mukherjee, P.; Zanni, M. T. *J. Phys. Chem. B* **2003**, *107*, 9165.
- (43) Becke, A. D. *J. Chem. Phys.* **1993**, *98*, 5648.
- (44) Perdew, J. P. *Phys. Rev. B* **1986**, *33*, 8822.
- (45) Hay, P. J.; Wadt, W. R. *J. Chem. Phys.* **1985**, *82*, 270.
- (46) Becke, A. D. *Phys. Rev. A* **1988**, *38*, 3098.
- (47) Lee, C.; Yang, W.; Parr, R. G. *Phys. Rev. B* **1988**, *37*, 785.
- (48) Wilson, E. B.; Decius, J. C.; Cross, P. C. *Molecular Vibrations*; McGraw-Hill: New York, 1955.
- (49) Zhao, Y.; Truhlar, D. G. *Acc. Chem. Res.* **2008**, *41*, 157.
- (50) Califano, S. *Vibrational States*; Wiley: New York, 1976.
- (51) Barone, V. *J. Chem. Phys.* **2005**, *122*, 014108.
- (52) Mukamel, S. *Principles of Nonlinear Optical Spectroscopy*; Oxford Series in Optical and Imaging Sciences; Oxford University Press: New York, 1999; Vol. 6.